Space Weather®

RESEARCH ARTICLE

10.1029/2024SW003993

Global Observations of Geomagnetically Induced Currents Caused by an Extremely Intense Density Pulse During a Coronal Mass Ejection

Terry Z. Liu[1], **Xueling Shi**[2,3], **Michael D. Hartinger**[1,4], **Vassilis Angelopoulos**[1], **Craig J. Rodger**[5], **Ari Viljanen**[6], **Yi Qi**[7], **Chen Shi**[1], **Hannah Parry**[8], **Ian Mann**[8], **Darcy Cordell**[8], **Hadi Madanian**[7], **Daniel H. Mac Manus**[5], **Michael Dalzell**[9], **Ryan Cui**[10], **Ryan MacMullin**[10], **Greg Young-Morris**[11], **Christian Noel**[11], and **Jeffrey Streifling**[11]

[1]Department of Earth, Planetary, and Space Sciences, University of California, Los Angeles, Los Angeles, CA, USA, [2]Department of Electrical and Computer Engineering, Virginia Tech, Blacksburg, VA, USA, [3]High Altitude Observatory, National Center for Atmospheric Research, Boulder, CO, USA, [4]Space Science Institute, Boulder, CO, USA, [5]Department of Physics, University of Otago, Dunedin, New Zealand, [6]Finnish Meteorological Institute, Helsinki, Finland, [7]Laboratory for Atmospheric and Space Physics, University of Colorado Boulder, Boulder, CO, USA, [8]Department of Physics, University of Alberta, Edmonton, AB, Canada, [9]Transpower New Zealand Ltd., Wellington, New Zealand, [10]AltaLink, Calgary, AB, Canada, [11]NB Power, Fredericton, NB, Canada

Key Points:

- A density pulse embedded in a coronal mass ejection drives global geomagnetic disturbances (GMD) and geomagnetically induced currents (GIC)
- Measured GIC's comparable to or exceed reference values in several regions, including 58.1 A in the mid-latitude region of United States
- Large-amplitude density pulses are an important driver of GIC and GMD for mid-latitude regions with large populations

Supporting Information:

Supporting Information may be found in the online version of this article.

Correspondence to:

T. Z. Liu, X. Shi and M. D. Hartinger,
terryliuzixu@ucla.edu;
xueling7@vt.edumhartinger@space-science.org;
mhartinger@spacescience.org

Citation:

Liu, T. Z., Shi, X., Hartinger, M. D., Angelopoulos, V., Rodger, C. J., Viljanen, A., et al. (2024). Global observations of geomagnetically induced currents caused by an extremely intense density pulse during a coronal mass ejection. *Space Weather*, *22*, e2024SW003993. https://doi.org/10.1029/2024SW003993

Received 9 MAY 2024
Accepted 13 SEP 2024

Author Contributions:

Conceptualization: Terry Z. Liu, Xueling Shi, Michael D. Hartinger
Data curation: Xueling Shi, Michael D. Hartinger, Craig J. Rodger, Ari Viljanen, Hannah Parry, Ian Mann, Darcy Cordell, Hadi Madanian, Daniel H. Mac Manus, Michael Dalzell, Ryan Cui, Ryan MacMullin, Greg Young-Morris, Christian Noel, Jeffrey Streifling
Formal analysis: Terry Z. Liu, Xueling Shi, Michael D. Hartinger

Abstract A variety of magnetosphere-ionosphere current systems and waves have been linked to geomagnetic disturbance (GMD) and geomagnetically induced currents (GIC). However, since many location-specific factors control GMD and GIC intensity, it is often unclear what mechanisms generate the largest GMD and GIC in different locations. We address this challenge through analysis of multi-satellite measurements and globally distributed magnetometer and GIC measurements. We find embedded within the magnetic cloud of the 23–24 April 2023 coronal mass ejection (CME) storm there was a global scale density pulse lasting for 10–20 min with compression ratio of ∼10. It caused substantial dayside displacements of the bow shock and magnetopause, changes of $6R_E$ and $1.3 - 2R_E$, respectively, which in turn caused large amplitude GMD in the magnetosphere and on the ground across a wide local time range. At the time this global GMD was observed, GIC measured in New Zealand, Finland, Canada, and the United States were observed. The GIC were comparable (within factors of 2–2.5) to the largest ever recorded during ≥14 year monitoring intervals in New Zealand and Finland and represented ∼2-year maxima in the United States during a period with several Kp ≥ 7 geomagnetic storms. Additionally, the GIC measurements in the USA and other mid-latitude locations exhibited wave-like fluctuations with 1–2 min period. This work suggests that large density pulses in CME should be considered an important driver of large amplitude, global GMD and among the largest GIC at mid-latitude locations, and that sampling intervals $\leq 10s$ are required to capture these GMD/GIC.

Plain Language Summary We explore how disturbances in the Earth's magnetic field, known as geomagnetic disturbances (GMD), and the resulting geomagnetically induced currents (GIC) in power systems are influenced by different electrical currents and waves in near-Earth space. One challenge is the lack of easily accessible data on GIC over long periods, which makes it hard to figure out what factors are most responsible for changes in GIC in different places. Also, there is limited research combining data from satellites with data collected on the ground to figure out exactly how GMD and GIC are generated. To tackle these issues, we looked at data collected by multiple satellites in different parts of near-Earth space along with data from ground magnetometers and GIC measurements distributed around the world. Our results suggest that density pulses from coronal mass ejections, a particular type of structure in the solar wind, are important in causing significant disturbances in the Earth's magnetic field globally and contribute to some of the largest GIC seen in the mid-latitude region of United States. We emphasize the importance of taking measurements with high sampling rates ($\leq 10s$) to accurately capture these disturbances and the resulting GIC.

1. Introduction

A variety of electric current systems and waves in the coupled solar wind-magnetosphere-ionosphere system cause variations in the magnetic field at the Earth's surface. These geomagnetic field variations induce electric field variations in the Earth, or geoelectric field variations. Geoelectric field variations in turn can drive

Funding acquisition: Terry Z. Liu, Xueling Shi, Michael D. Hartinger
Investigation: Terry Z. Liu, Xueling Shi, Michael D. Hartinger, Vassilis Angelopoulos, Craig J. Rodger, Ari Viljanen, Yi Qi, Chen Shi, Hannah Parry, Ian Mann, Darcy Cordell, Hadi Madanian, Daniel H. Mac Manus, Michael Dalzell, Ryan Cui, Ryan MacMullin, Greg Young-Morris, Christian Noel, Jeffrey Streifling
Methodology: Terry Z. Liu, Xueling Shi, Michael D. Hartinger
Supervision: Vassilis Angelopoulos
Validation: Terry Z. Liu, Xueling Shi, Michael D. Hartinger
Visualization: Terry Z. Liu, Xueling Shi
Writing – original draft: Terry Z. Liu, Xueling Shi, Michael D. Hartinger
Writing – review & editing: Terry Z. Liu, Xueling Shi, Michael D. Hartinger, Vassilis Angelopoulos, Craig J. Rodger, Ari Viljanen, Yi Qi

geomagnetically induced currents (GIC) that are capable of damaging power grids, telecommunications cables, and oil and gas pipelines, as well as disrupting railroad switching systems (e.g., Patterson et al., 2023; Pilipenko, 2021; Pulkkinen et al., 2017). The intensity of the GIC for a particular geomagnetic field variation depends on several factors, including the amplitude/frequency/polarization/duration of the geomagnetic field variations, the local electrical conductivity of the Earth, and the configuration of the power system that the GIC flows through (e.g., Love et al., 2019; Lucas et al., 2020; Shi et al., 2022; Zheng et al., 2014).

A particular geomagnetic field variation may lead to GIC that cause damage/disruptions to power systems in some situations and GIC that have no impacts on power systems in others. For example, the electrical conductivity of the Earth is a major factor controlling the amplitude of both geoelectric field and GIC (e.g., Cordell et al., 2021; Love et al., 2018), and it varies significantly from location to location; thus geoelectric hazard maps indicate that at fixed geomagnetic field variation amplitude, certain regions are much more likely to have large amplitude thus potentially hazardous geoelectric fields and GIC (e.g., Love et al., 2022). The particular network topology, power system configuration, and its susceptibility to GIC which is primarily contingent upon the characteristics of the transformers involved, are also important. Reference values for geomagnetic field variation, geoelectric field variation, and GIC are thus important for assessing whether a particular event might represent a hazard. These values may be based on long-term monitoring (e.g., Rodger et al., 2017; Viljanen et al., 2010) or observations from past events representing major geomagnetic storms that may have been linked to a power system failure, transformer failure, etc., or a combination (e.g., Love et al., 2023). While geomagnetic and geoelectric field values can be generalized, GIC reference values cannot typically be generalized from one type of power system to another or from one power grid to another. For example, a reference GIC value for a gas pipeline would not be applicable to a power grid, or vice versa. Table 1 provides reference values for GIC for a few different power grids and a gas pipeline in Finland taken from long-term monitoring intervals and/or recent geomagnetic storms. Although the GIC reference values from Table 1 have different reference types (e.g., length from 2 to 25 years) and are not directly comparable, they provide important context to the event-specific GIC measurements shown in this study.

There are a multitude of different magnetosphere-ionosphere current systems and waves that have been linked to hazardous GMD and GIC (e.g., Hartinger et al., 2023; Juusola et al., 2023; Schillings et al., 2022). Some of these phenomena are associated with global geomagnetic disturbance (GMD) seen at a wide range of latitudes and longitudes (e.g., Fiori et al., 2014; Love et al., 2023; Marin et al., 2014), while others are more localized (e.g., Apatenkov et al., 2020; Espinosa et al., 2019). Reports of the most intense GIC, including those that have been linked to power system disruptions, are often associated with geomagnetic storms caused by coronal mass ejections (CME). During CME-storms, intense GIC have been linked to the initial arrival of the CME (e.g., Oliveira et al., 2024), that is, the impact of the CME's interplanetary shock on the Earth's magnetosphere; this creates several types of magnetic latitude and longitude dependent current systems and waves (Araki, 1994). Although the GMD associated with these shocks have amplitudes that vary with spatial location including some locations having very weak GMD, they are often referred to as a "global" response since, in contrast to more localized mesoscale current systems (spatial scale <500km) or large scale current systems confined to a narrow range of local times or latitudes, the GMD related to these currents/waves are measurable at a wide range of local times and latitudes. Hereafter, we shall use the same convention when referring to GMD as being "global." Intense GIC have also been linked to disturbances within the CME-sheath that arrive after the interplanetary shock, including fluctuations in the CME (Kilpua et al., 2019) that create global GMD. Finally, CMEs are often associated with intense magnetic fields with favorable orientation (opposite to the Earth's magnetic field direction, i.e., southward interplanetary magnetic field, IMF) for magnetic reconnection that in turn causes intensification of global plasma transport, ring current intensification, increased nightside reconnection, and the intensification and equatorward expansion of auroral electrojets. Many of these effects have been linked to GMD and intense GIC; for example, nightside auroral electrojet intensifications have been linked to power grid disruptions during the March 1989 storm in Quebec (Boteler, 2019).

While most studies of GIC related to CME have focused on interplanetary shocks (sudden impulse) and on periods with intense southward IMF (e.g., Smith et al., 2024), other structures related to CME may also drive potentially hazardous GIC. This includes pressure-balanced density pulses, which can be mirror mode and slow mode in nature, frequently observed in the solar wind and sheath region of CMEs (e.g., Ala-Lahti et al., 2018; Chandrasekhar et al., 1958; Dimmock et al., 2015, 2022; Hasegawa, 1969; He et al., 2015; Howes et al., 2012; Narita & Marsch, 2015; Tu & Marsch, 1995). Both modes are fundamental plasma phenomena, characterized by

Table 1
Geomagnetically Induced Currents (GIC) Reference Values Compared to Maximum GIC in This Study

Study	Magnetic latitude (°)	Power system type	Reference type	GIC (Amperes)
Rodger et al. (2017)	−50.09	NZ Power Grid	14-year	34.1
		Transformer ISL M6	Maximum	
This Study, 24 April 2023 storm	−49.95	NZ Power Grid	Event	16.2
		Transformer ISL M6	Maximum	
Altalink Maximum Reported 2022–2023		AB Power Grid	Seven Storms	
	60.0	Transformer 320P	Kp > 6 in 2022–2023	131
	57.5	Transformer 520S		28
This Study, 24 April 2023 storm	60.0	Transformer 320P	Event	64
	57.5	Transformer 520S	Maximum	15
NB Power Maximum Reported	54.56	Canada Power Grid	Four Storms	24.8
Recent Storms Kp ≥ 7		Transformer (10628)	Kp ≥ 7 in 2022–2023	
This Study, 24 April 2023 storm	54.56	Canada Power Grid	Event	24.8
		Transformer (10628)	Maximum	
ATC Maximum Reported	51.75	US Power Grid	~2-year	58.1
November 2021–January 2024		Transformer (10659)	Maximum	
ATC Maximum Reported	51.75	US Power Grid	Two Storms	58.1
Recent Storms Kp≥7		Transformer (10659)	Kp ≥ 7 in 2023	
This Study, 24 April 2023 storm	51.75	US Power Grid	Event	58.1
		Transformer (10659)	Maximum	
Viljanen et al. (2010), extended-2023	~57–58	Finland Gas	25-year	57
		Pipeline	Maximum	
This Study, 24 April 2023 storm	57.35	Finland Gas	Event	35
		Pipeline	Maximum	

anti-correlation between the magnetic field strength and density, on MHD or kinetic scales. Associated with field strength depletion, the density enhancement and thus dynamic pressure enhancement could lead to back-and-forth motion of the bow shock and magnetopause, and thus create GMDs (e.g., Sibeck, 1990) including pulsations, also referred to as ultra low frequency (ULF) waves.

There is still debate on which phenomena can lead to potentially hazardous GIC (i.e., can potentially cause damage/disruption to power systems), and recent work suggests that the answer can change from storm to storm. For example, power system failures in Quebec during the March 1989 storm were attributed to an auroral electrojet on the nightside (Boteler, 2019), while other studies suggest that dayside phenomena related solar wind disturbances related to interplanetary shocks, the impact of multiple CMEs, and quasi-periodic variations may lead to power system disruptions and/or damage during the 1940 and 2003 storms (Love et al., 2023; Pulkkinen et al., 2005). It is crucial to identify which specific mechanisms—whether CME-related or not—can drive potentially hazardous GIC, and at which locations intense GIC might occur for a given mechanism. This information is needed to improve both physics-based models (e.g., to ensure model configurations are appropriate for capturing the relevant phenomena) and data-driven models (e.g., to ensure the measurements constraining the models are captured at the appropriate spatial and temporal resolution and in the appropriate locations).

In this study, we examine the drivers of global GMD as well as observations of GIC at several widely distributed locations during the 23–24 April 2023 CME-storm, focusing on the impact of a large density pulse embedded within the CME. In particular, we analyze multi-satellite measurements in the solar wind, magnetosheath, magnetosphere, as well as globally distributed magnetometer and GIC measurements, with the GIC measurements referenced against long monitoring intervals and past geomagnetic storms. As we shall show, (a) the CME-density pulse led to among the largest, or in some cases the largest, GIC values reported at mid-latitude locations, and (b) these GIC exhibited fluctuations with 1–2 min periodicity at some locations during this time period. This suggests that large density pulses in CME should be considered an important driver of large amplitude, global GMD and among the largest GIC at mid-latitude locations, and that sampling intervals $\leq 10s$ are required to capture these GMD/GIC.

2. Data Sets

We use observations from the Magnetospheric Multiscale mission (MMS) (Burch et al., 2016) and Time History of Events and Macroscale Interactions during Substorms mission (THEMIS) (Angelopoulos, 2008) in the dayside region, as well as the ARTEMIS mission (TH-C spacecraft) at lunar orbit which was part of THEMIS before 2010. Plasma data from the MMS fast plasma investigation (FPI) instrument suite (Pollock et al., 2016) and the THEMIS electrostatic analyzer (ESA) (McFadden et al., 2008) and direct current (DC) magnetic field data from fluxgate magnetometer onboard MMS (Russell et al., 2016) and THEMIS (Auster et al., 2008) are used. Ion composition is measured from MMS Hot plasma composition analyzer (HPCA) (Young et al., 2016). We also use Deep Space Climate Observatory (DSCOVR) observations at L1 (Loto'aniu et al., 2022) and Korean Multi-Purpose Satellite (KOMPSAT) magnetometer observations at geosynchronous orbit (Kim, 1999; Magnes et al., 2020).

As noted in Section 1, the GIC in a given power system depends on many factors including spatial and temporal GMD variations, local ground conductivity, and power system configuration and resistances. To explore and quantify a range of GIC responses that are possible, we examine GIC data from multiple widely spread sites, all referenced against extended monitoring intervals or past storms. This type of analysis is rarely conducted (e.g., Clilverd et al., 2021); most past studies showing GIC measurements examine a single geographic region/power system and/or do not reference their results. The GIC data used in this study from multiple different sources as listed below:

1. Finland: recordings of GIC in the Finnish natural gas pipeline are carried out close to the Mäntsälä compressor station in southern Finland (60.6°N, 25.2°E).
2. North American Electric Reliability Corporation (NERC) GMD database: The NERC GMD database includes North American GIC monitor and ground magnetometer data during geomagnetic storms of $\mathrm{Kp} \geq 7$. GIC data from two sites (device 10659 and 10628) are used in this study. Device 10628 is operated by New Brunswick Power in Eastern Canada; it corresponds to an ECLIPSE GIC monitoring device from Advanced Power Technologies. The measurement is taken with a split-core Hall-effect CT. The other device 10659 is operated by American Transmission Company, LLC in the Upper Midwest region of the United States; it also corresponds to a split-core Hall sensor. This monitor (device 10659) runs with an offset DC value of about 5 A which was subtracted during the analysis in this study.
3. Alberta: GIC in Alberta is measured by AltaLink on transformers at Keephills substation (320P) in central Alberta and Bennett substation (520S) in southern Alberta. The GIC sensors used by AltaLink are also ECLIPSE GIC monitoring devices from Advanced Power Technologies, the same as those used by New Brunswick Power. For more information on the GIC measurements see Cordell et al. (2024).
4. New Zealand: GIC measurements from Transpower New Zealand Limited consisting of DC measured in several transformers in the South Island of New Zealand. Data from the Islington (ISL) number 6 transformer are used for this study as ISL is close to the EYR magnetometer; the measurements at this transformer are referred to as ISL M6. For further details on this GIC data set, see Mac Manus et al. (2017), Rodger et al. (2020), and Clilverd et al. (2020).

To assess the ground response, we use ground magnetometer data from Finnish Meteorological Institute (FMI) with 1-s cadence, several networks that are obtained from the SuperMAG database with 1-min cadence in standard SuperMAG format (Gjerloev, 2012), and MAGStar with 1-s cadence (Gannon, 2023). Ground magnetic field perturbations (ΔB) are obtained by subtracting their mean within the time interval showed in each figure. The time derivative of horizontal magnetic field perturbations (dH/dt) is obtained from $dH/dt = \sqrt{dB_x/dt + dB_y/dt}$.

3. Results

On 23–24 April 2023, a CME caused a geomagnetic storm. The storm had a minimum in Dst of −213 nT (provisional Dst index obtained from WDC for Geomagnetism, Kyoto, https://wdc.kugi.kyoto-u.ac.jp/dst_provisional/202304/index.html), which is considered intense, though not among the most extreme geomagnetic

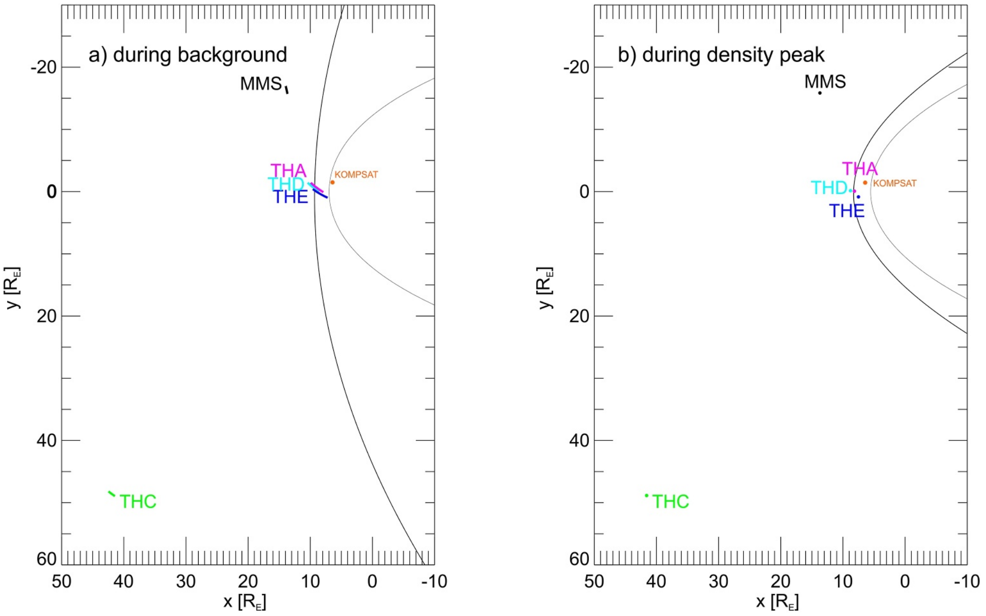

Figure 1. Spacecraft positions relative to the bow shock and magnetopause before and during the density peaks. The Merka et al. (2005) bow shock model and Shue et al. (1998) magnetopause model are used. Because of the extreme upstream conditions (e.g., very low Alfvén Mach number), the model bow shock shape may be unrealistic.

storms ever reported (Gonzalez et al., 1994). Recent studies by Despirak et al. (2023), Ghag et al. (2024), and Zou et al. (2024) have examined this CME and/or corresponding GMD and GIC responses; we discuss some of these results in later sections. For now, we note that some of these studies have labeled 23–24 April 2023 as being two geomagnetic storms (Despirak et al., 2023), while others have labeled this as a single two-step geomagnetic storm (Ghag et al., 2024); these studies are referring to the fact that Dst has two distinct minima likely related to the time evolution of IMF Bz (note that two geomagnetic storms are not necessarily related to two CMEs). Whether this event is labeled a single two-step geomagnetic storm or two separate geomagnetic storms matters little to the present work. We focus on one particular time interval near the time of the second Dst minimum at 6 UT on 24 April 2023.

3.1. Upstream Analysis

In this subsection we focus on a transient scale structure during this CME event, while following subsections will examine global GMD and GIC. TH-C at lunar orbit (see position in Figure 1) observed that there was a sharp density gradient at ∼01:30 UT that decreased the plasma density to $\sim 2-6\ cm^{-3}$ (Figure 2c) while the IMF strength remained ∼30 nT (Figure 2a), signifying a transition from CME sheath to magnetic cloud (Ghag et al., 2024). At 03:30–03:50 UT, there were two density peaks of greater than 40 cm^{-3} (Figure 2c) with slight field strength decrease (Figure 2a). As a result, the dynamic pressure increased by a factor of more than 10 (Figure 2e). Similar observations were also seen by DSCOVR (Figure S1 in Supporting Information S1), ACE, and Wind (not shown). Thus, this structure was not locally formed but already existed at least before L1. As the variations of IMF magnitude and plasma parameters are inconsistent with an interplanetary shock (as seen from Figure 2 and Figure S1 in Supporting Information S1), we call it an extremely intense density pulse.

Corresponding to the two density peaks, the ion energy flux shows clear enhancement at ∼7 keV (Figure 2b). This flux enhancement is from heavy ions based on ion distribution functions (just like the secondary beam at ∼3 keV from alpha particles) because ESA instrument assumes all ions to be protons causing the energy of heavy ions to be overestimated by a factor of mass-to-charge ratio (4–5 in this case). The appearance of these heavy ions in the energy spectrum could be either due to the extremely intense density enhancement that increased their flux to above the instrument noise level or due to a source of heavy ions associated with the structure.

MMS around the dawn flank (Figure 1) observed the response of the bow shock. Figure 3 shows that MMS was initially in the solar wind, and then due to the density and thus dynamic pressure decrease observed by TH-C (a

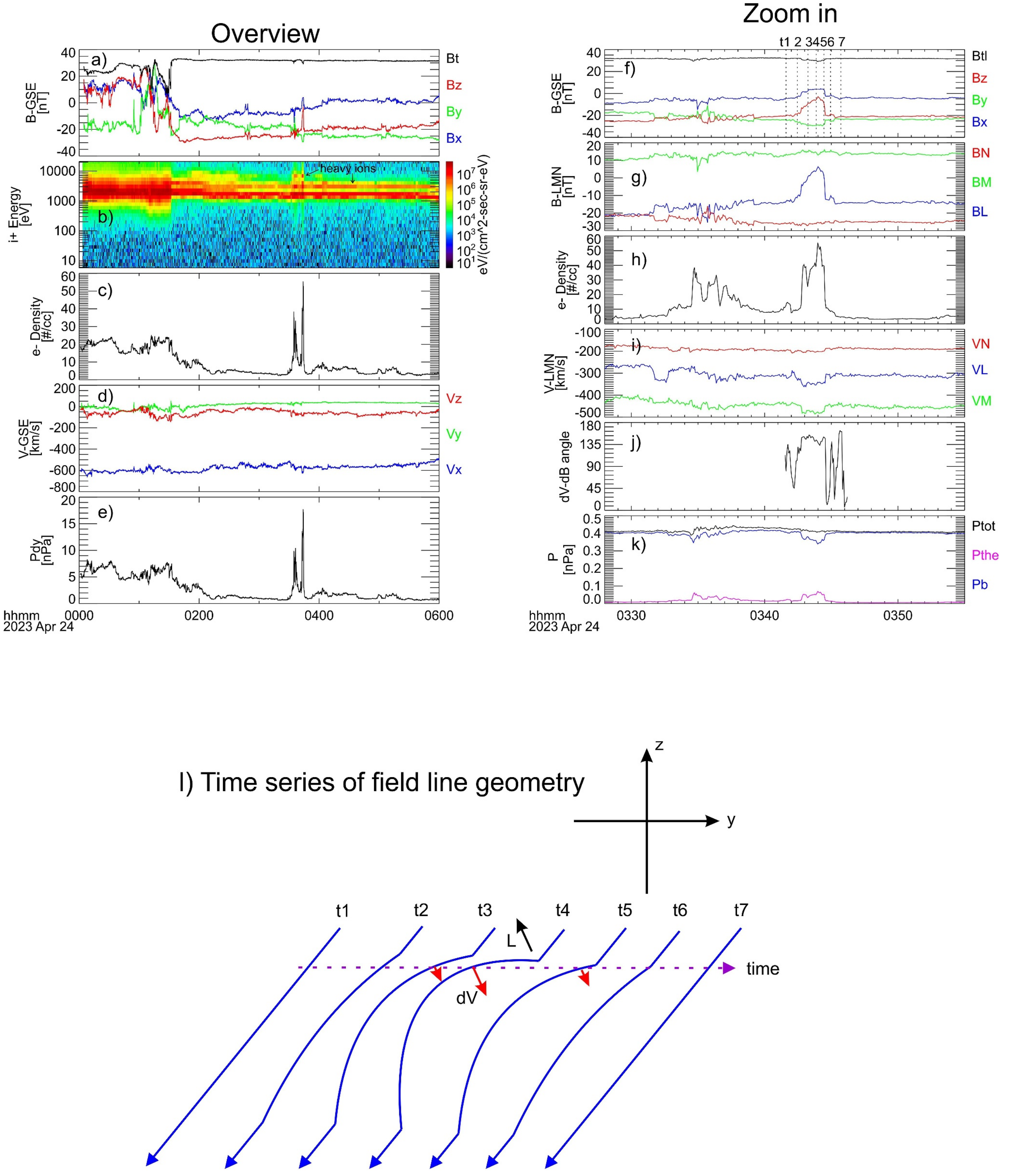
Overview
a)
B-GSE [nT]
40
20
0
-20
-40
Bt
Bz
By
Bx
b)
i+ Energy [eV]
10000
1000
100
10
heavy ions
10^7
10^6
10^5
10^4
10^3
10^2
10^1
eV/(cm^2-sec-sr-eV)
c)
e- Density [#/cc]
60
50
40
30
20
10
0
d)
V-GSE [km/s]
200
0
-200
-400
-600
-800
Vz
Vy
Vx
e)
Pdy [nPa]
20
15
10
5
0
hhmm
2023 Apr 24
0000
0200
0400
0600
Zoom in
t1 2 3456 7
f)
B-GSE [nT]
Btl
Bz
By
Bx
g)
B-LMN [nT]
20
10
0
-10
-20
-30
BN
BM
BL
h)
e- Density [#/cc]
i)
V-LMN [km/s]
-100
-200
-300
-400
-500
VN
VL
VM
j)
dV-dB angle
180
135
90
45
0
k)
P [nPa]
0.5
0.4
0.3
0.2
0.1
0.0
Ptot
Pthe
Pb
hhmm
2023 Apr 24
0330
0340
0350
l) Time series of field line geometry
z
y
t1
t2
t3
t4
t5
t6
t7
L
dV
time

Figure 2.

sharp decrease at ~01:30 UT and gradual decrease later on in Figures 2c and 2e), the bow shock moved outward causing MMS to enter the magnetosheath. Later, because of the density pulses and the associated significant dynamic pressure enhancement, the bow shock was pushed back, and MMS observed the first density peak interacting with the bow shock and the second density peak in the solar wind. After the density peaks, there was back-and-forth motion of the bow shock as well as density and velocity perturbations in the magnetosheath caused by the solar wind density/dynamic pressure perturbations (Figures 2c and 2e). Similar to TH-C observations, MMS also observed the flux enhancement of heavy ions at the second density peak (also see ion distributions in Figure S2 in Supporting Information S1).

Zooming in and transforming to the local LMN coordinates using minimum variance analysis (MVA, Sonnerup & Scheible, 1998) on the magnetic field around the second density peak, TH-C (Figure 2g), MMS (Figure 3g), and DSCOVR (Figure S1g in Supporting Information S1) observed the same field variation: a unipolar B_L variation without any clear change in B_M and B_N (thus we cannot trust M and N direction). Using the timing method between TH-C and MMS in the direction perpendicular to the L direction (e.g., Schwartz, 1998), we calculate that the structure normal is mostly along GSE-X (~[0.89, 0.26, −0.36]). Based on the field variation and spacecraft crossing direction, we construct the field geometry of this structure in Figure 2l.

Initially (t1 in Figure 2l), the IMF lines were mostly in the -Y and -Z direction in GSE. While crossing the structure (mostly along GSE-X direction perpendicular to the field), the field lines became more and more curved leading to more negative B_y and less negative B_z (t2–t4 in Figure 2l). After crossing the center (t4–t7), the field lines gradually changed back to the background geometry (The first density peak shows similar field variation except in the opposite direction.). Based on the field geometry, the structure is consistent with a magnetic bottle in the YZ plane with thickness along GSE-X of ~17 R_E (3 min × 600 km/s), which confined plasma within it. Because all TH-C, MMS, and DSCOVR observed similar field variation with spatial separation in the GSE-YZ plane by ~70 R_E, such a magnetic bottle should be elongated along the field lines by a very long distance compared to the transect.

The ion bulk velocity shows variation in a direction opposite to that of the magnetic field variation (see L component in Figures 2j and 3j, and Figure S1j in Supporting Information S1). As sketched in Figure 2l, such velocity variation indicates that the curved field lines tended to recover. Thus, this structure was very likely dissipating. Note that, the V_M enhancement in Figures 2i and 3i corresponding to V_X enhancement in Figures 2d and 3d was mostly due to the appearance of heavy ions with energy/bulk speed overestimated by ESA and FPI instruments (DSCOVR did not observe such a V_M or V_X enhancement as Faraday Cup measurement is more accurate than ESA and FPI).

Figures 2k and 3l show that the magnetic pressure decrease (blue) can be almost balanced by the electron thermal pressure enhancement (magenta). Because ESA and FPI cannot measure solar wind ion temperature correctly, the ion thermal pressure is not shown. DSCOVR observations show that due to ion temperature decrease, the ion thermal pressure decreased to a very small value within the structure (Figure S1k in Supporting Information S1). Overall, this was roughly a pressure balanced structure. Thus, the extremely intense density enhancement was likely due to the very low plasma β (on the order of 0.1) that even a slight magnetic pressure decrease, the plasma density had to increase significantly to balance it.

Because of the magnetic bottle-like geometry and anti-correlation between the magnetic field strength and density with balanced pressure, the nature of this structure was very likely a mirror mode or slow mode. If it was a mirror mode, there should be strong perpendicular temperature anisotropy within the structure. Figure 3k shows significant enhancement in ion perpendicular temperature compared to parallel temperature, even though field strength depletion tended to cause betatron cooling. This can also be seen by comparing ion/proton distributions

Figure 2. TH-C observations of the event. The top left plot shows the overview of the event. From top to bottom are (a) magnetic field in GSE, (b) ion energy spectrum, (c) electron density, (d) ion bulk velocity in GSE, (e) dynamic pressure. The top right plot is the zoom-in plot of the density peaks. From top to bottom are (f) magnetic field in GSE, (g) magnetic field in LMN coordinates, (h) electron density, (i) ion bulk velocity in LMN coordinates, (j), the angle between the magnetic field variation and velocity variation (by subtracting the ambient background), (k) magnetic pressure (blue), electron thermal pressure (magenta), and the sum (black). The sketch on the bottom indicates the magnetic field line shapes (blue arrows) in the GSE-YZ plane (not a 3D plot), at different time (t1–t7 in panel f) when the spacecraft cross it. The dotted arrow is time axis, and its crossing at the field lines indicate the locally observed field line direction in the GSE-YZ plane. The field line shapes are sketched based on the assumption that the field lines are eventually along the background field direction far away from the perturbations. The short black arrow indicates the L direction (maximum variation direction) and red arrows indicate the velocity variation direction.

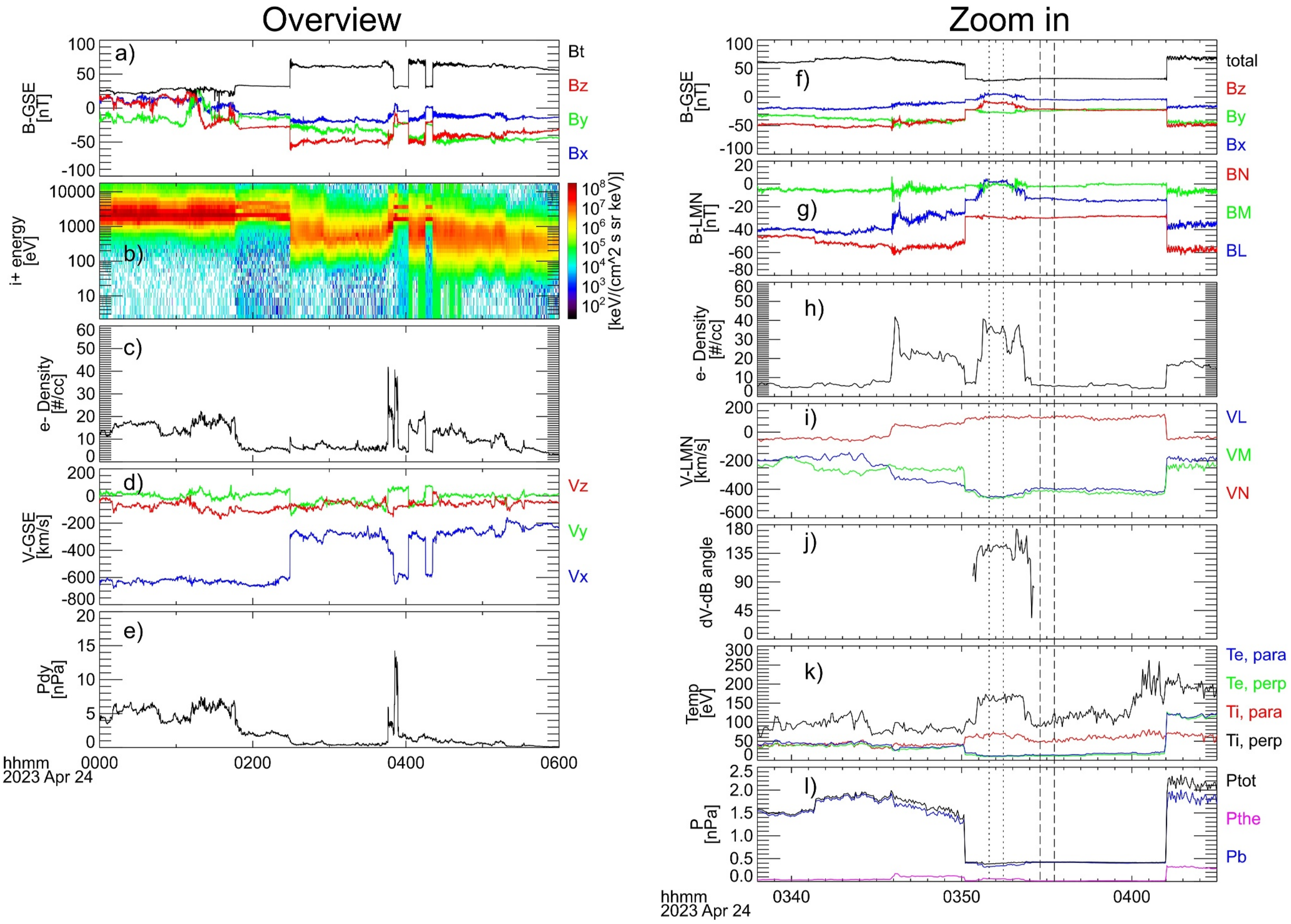

Figure 3. Magnetospheric Multiscale mission observations of the event. The left and right plots are in a similar format as Figure 2, except that the electron and ion temperature in the perpendicular and parallel directions are shown in panel (k). Time intervals between two vertical dotted lines and dashed lines in the right plot are for ion distributions from fast plasma investigation and hot plasma composition analyzer in Figure S2 in Supporting Information S1.

inside the density peak and the nearby background (corresponding to dotted and dashed vertical lines, respectively), measured from FPI and HPCA instruments (Figure S2 in Supporting Information S1). Thus, the perpendicular temperature anisotropy of ions might be the free energy source of the structure. However, FPI measured protons were convolved with the heavy ions, and the HPCA instrument requires special processing for deadtime corrections during the event, so these results have to be treated with caution.

Because the plasma β was very low (~0.1), to satisfy the mirror mode criterion ($T_{\perp}/T_{\parallel} > 1 + 1/\beta$; Hasegawa, 1969), the perpendicular temperature should be more than 10 times the parallel temperature, which can be hardly achieved. One possible cause of this inconsistency is that this structure was a remnant of a mirror mode structure formed when the plasma β was not low. While it was propagating toward L1 and Earth, the structure started to dissipate as suggested by the velocity variation direction opposite to that of the field. Another possibility is that this structure may be a slow mode (e.g., He et al., 2015; Narita & Marsch, 2015), which can exist at a low plasma β environment. Its wave vector direction could be quasi-perpendicular to the background field (mostly in the YZ plane) so that it was quasi-static. Additionally, modeling by L. Zhang et al. (2018) suggested that such a kind of structures could be a mixture of mirror mode and slow mode.

Mirror modes and slow modes are very common across the heliosphere (e.g., Ala-Lahti et al., 2018; He et al., 2015; Howes et al., 2012; Winterhalter et al., 1994; T. L. Zhang et al., 2009). The complicated plasma environments, such as around CMEs, could sometimes cause them to have extreme density/dynamic pressure variations. Several more examples can be found in Supporting Information S1. Such extremely intense dynamic

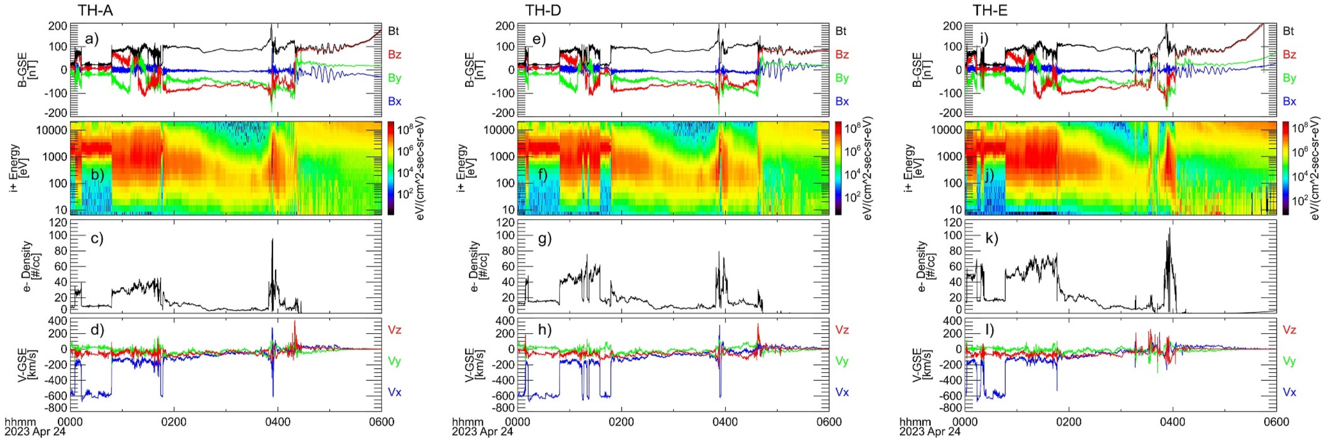

Figure 4. Three Time History of Events and Macroscale Interactions during Substorms mission observations of the event. From top to bottom are magnetic field in GSE, ion energy spectrum, electron density, and ion bulk velocity.

pressure variations can lead to significant bow shock and magnetopause back-and-forth motion as demonstrated in the next section.

3.2. Downstream Response

During this event, three THEMIS spacecraft (TH-A, TH-D, and TH-E) were around the subsolar region (Figure 1). They were initially in the solar wind and crossed the bow shock at $X \sim 11R_E$ at ~00:50 UT. Right before the arrival of the sharp density gradient observed by TH-C, three THEMIS spacecraft observed back-and-forth motion of the bow shock (~01:40–01:50 UT). Due to the sharp density/dynamic pressure decrease, the bow shock moved outward globally. After the three spacecraft entered the magnetosheath again at ~01:50 UT, they observed the gradual decrease in plasma density (Figures 4c, 4g, and 4k), speed (Figures 4d, 4h, and 4l and see decreasing energy in Figures 4b, 4f, and 4j), and temperature (see narrower energy band in Figures 4b, 4f, and 4j). Such plasma parameter variations were caused by the gradual expansion of the bow shock/magnetosheath due to the gradual density/dynamic pressure decrease observed by TH-C. Due to the global expansion as well as the extremely low Alfvén Mach number ($\sim 1-3$), the magnetosheath density was even closer to the solar wind density. Such global expansion caused MMS to cross the bow shock at $X \sim 13.9R_E$ around the flank at ~02:30 UT (so the bow shock nose should be at $X > 13.9R_E$).

At ~03:40 UT, TH-E temporarily crossed the magnetopause into the magnetosphere at $X \sim 7.7R_E$ likely due to the global expansion. Then the two large density peaks encountered the bow shock causing TH-A and TH-D to suddenly enter the solar wind at $X \sim 8R_E$. Because MMS crossed the flank bow shock at $X \sim 13.7 - 13.9R_E$ before and after the density peaks, the bow shock nose moved back-and-forth by more than 6 R_E driven by the density peaks (The time delay between MMS and THEMIS is consistent with the normal of density peaks.) Meanwhile, KOMPSAT at $X \sim 6.4R_E$ around noon (Figure 1) entered the magnetosheath from the magnetosphere and back (Figure 5d), meaning that the magnetopause moved inward by more than 1.3 R_E, up to $\sim 2R_E$ estimated from the time delay from TH-E to KOPMSAT and to the center time in the magnetosheath. Because the bow shock moved inward more significantly than the magnetopause, the dayside magnetosheath was compressed leading to field strength enhancement up to ~200–250 nT as observed by TH-E and KOMPSAT (Figures 5c and 5d). The compression by a factor of ~2–2.5 was roughly consistent with the estimated thickness decrease of the subsolar magnetosheath (from ~6.2 to 2.2 R_E based on the bow shock and magnetopause displacements discussed above).

Such extreme back-and-forth motion of the bow shock within a short time drove significant phenomena in the magnetosphere and ionosphere as well as on the ground seen from large geomagnetic field perturbations (~500 nT in Figure 5e and ~10 nT/s in Figure 5f) and GIC (~60 A in Figure 5g) in the United States. These measurements from the HET ground magnetometer from the MAGStar array and NERC GIC site device 10659 were located in the pre-midnight sector slightly below 55° MLAT and shown as green dot (HET) and red triangle (Device 10659) in Figure 6. More details on the ground response will be shown in the next section.

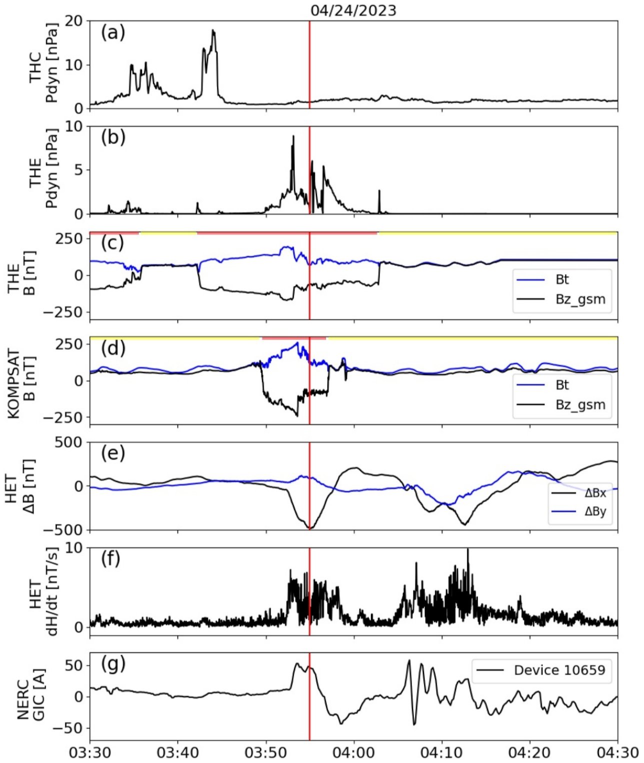

Figure 5. Time History of Events and Macroscale Interactions during Substorms mission observations and ground response to the upstream magnetic bottle structure. From top to bottom are (a) THC dynamic pressure, (b) THE dynamic pressure, (c) THE total magnetic field (B_t, blue line) and the northward component (B_z, black line) in GSM coordinates, (d) Korean Multi-Purpose Satellite total magnetic field (B_t, blue line) and the northward component (B_z, black line) in GSM coordinates, (e) horizontal geomagnetic field perturbations (black: ΔB_x and blue: ΔB_y) from the HET ground magnetometer, (f) the time derivative of horizontal magnetic field perturbations (dH/dt) from the HET ground magnetometer, (g) geomagnetically induced currents (GIC) measurements at device 10659 from the NERC GMD database. The pink and yellow bars in panels (c, d) indicate the time intervals when the satellite was located in the magnetosheath and magnetosphere, respectively. The vertical red line marks 03:55 UT, the moment when multiple sites detected an enhanced GIC.

After the density peaks, THEMIS crossed the magnetopause and observed clear northward flow (Figures 4d and 4h). This was very likely magnetopause reconnection outflow due to the southward IMF. In the magnetosphere, clear magnetospheric ULF waves were observed with oscillation predominantly in the radial direction, likely caused by the global back-and-forth motion of the magnetopause. The magnetic reconnection and the ULF waves are beyond the scope of this study and are a topic for future work. However, another type of shorter period ULF wave activity will be discussed in the context of GMD and GIC in the next subsection.

3.3. Ground Response: Geomagnetic Disturbances and GIC

Measurements from multiple widely spread ground magnetometers and GIC sites as shown in Figure 6 are used to investigate the ground response (GMDs and GIC) to the upstream density pulse structure. The black dots clustered around dawn indicate locations of ground magnetometers from the FMI. The blue dots widely spread in local time are ground magnetometers located at 57-60° MLAT in the evening sector that detected the strongest geomagnetic field perturbations at their specific local times (see Figure 8 and the corresponding text for more details). Red triangles show GIC sites from Finland (dawn) and North America (pre-midnight to midnight). The red diamond shows the conjugate magnetic footprint of the New Zealand ISL M6 site located in the afternoon sector at 03:50 UT on 24 April 2023. While we don't focus on dayside ground-based observations due in part to a lack of coverage in the latitudinal range shown in Figure 6 and our desire to focus on regions where GIC measurements are available and large GIC were observed, we can at least say that large dayside GMD would be expected given (a) the dayside satellite observations that showed the large inward magnetopause displacement (previous section) and (b) theory, modeling, and observation that have all linked such large solar wind density/pressure pulses and magnetopause excursions to global GMD including on the dayside (Araki, 1994; Sibeck, 1990) and (c) low-latitude stations in India, Vietnam, and other locations (Figure S7 in Supporting Information S1) at the time of the density pulse showing a clear GMD response consistent with expectations from past theory, modeling, and observation studies.

A latitudinal ground magnetometer chain from the FMI array (black dots in Figure 6) is used to study the dawn sector latitudinal dependence of the magnetic field perturbations and shown in Figure 7. The strongest magnetic field perturbations ($\Delta B \geq 1{,}000$ nT) were observed to be localized between 58 and 60° MLAT around dawn. These perturbations are characterized by a negative bay mainly in the northward magnetic field component (black line) lasting for ≤10 min. This magnetic depression suggests a strong westward electrojet in the dawnside ionosphere. For ground magnetometers located above the MEK site at 60° MLAT and below the NUR site at 58° MLAT, the magnetic field perturbations are much weaker compared to the three sites (MEK, HAN, and NUR) located between 58 and 60° MLAT.

A longitudinal ground magnetometer chain at about 57–60° MLAT from SuperMAG (blue dots in Figure 6, this includes data from several individual magnetometer networks obtained from the SuperMAG database) is used to study the local time dependence of the magnetic field perturbations and is shown in Figure 8. This narrow range of latitudes was chosen to explore whether the latitudinally localized disturbance seen at dawn extended to other local time sectors. The largest perturbations are observed by the DOB site (~2,000 nT) located at ~5 hr MLT. Note that we use the 1-min cadence SuperMAG data in Figure 8, therefore the actual perturbation amplitude could be larger since some phenomena may be undersampled or eliminated in 1-min data (Hartinger et al., 2023; Trichtchenko, 2021). It can also be seen that the magnetic field perturbations (mainly in the northward component from a local magnetic coordinate system) are much stronger in the post-midnight sector compared to the pre-midnight sector. To summarize, the overall ground magnetic field perturbations in

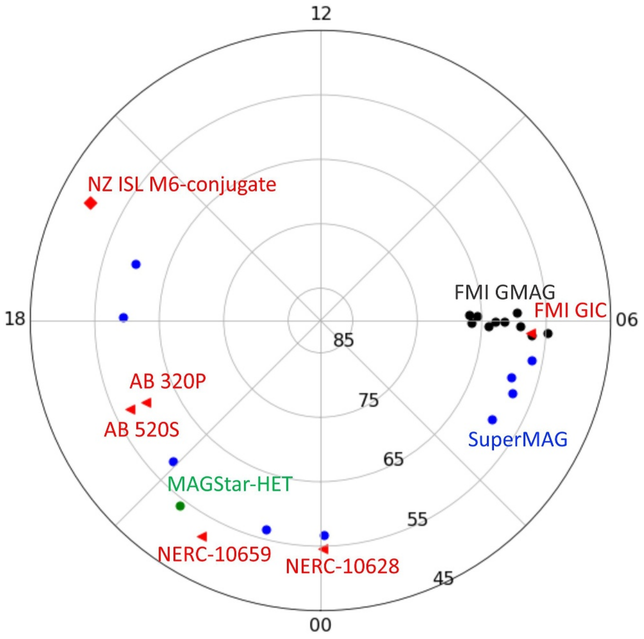

Figure 6. MLAT-MLT map shows the location of ground instruments used in this study at 03:50 UT on 24 April 2023. Black dots show Finnish Meteorological Institute ground magnetometers; blue dots show a longitudinal chain at 58–62° MLAT from SuperMAG; red triangles show geomagnetically induced currents sites from Finland and North America (US and Canada); red diamond shows the conjugate footprint of the New Zealand ISL M6 site.

response to the upstream density pulse are global with the largest perturbations observed around the dawn at ~60° MLAT. These results are consistent with results from Zou et al. (2024) reporting an extreme auroral electrojet spike during the same 24 April 2023 storm. Stated another way, the density pulse created an overall global response based on both satellite and ground-based observations spanning the dayside and nightside, with more locally intense GMD in some regions due, for example, to the presence of an intense auroral electrojet.

GIC measurements from multiple sites across the world including Finland, United States, Canada, and New Zealand are shown in Figure 9. With the exception of the top panel for the Finnish gas pipeline, all other panels are for measurements related to power grids. As can be seen from Figure 9, GIC measurements from Finland (dawnside), North America (US and Canada on the nightside), and New Zealand (afternoon) all have a clear response to the upstream solar wind density pulse. Note that the New Zealand GIC measurements from the southern hemisphere (panel (f)) respond almost simultaneously with the Finnish (panel (a)) and North American (panel (b–d)) GIC without significant time delay, with amplitudes ranging from ~15–65 A. There are notable differences in amplitude and time dependence between the different GIC measurements shown in the panels of Figure 9. These differences are due to many factors, including the interplay between the spatial variations of the GMD related to the density pulse, the directional biases of each network, and more (see next paragraph). Detailed analysis of all factors is an important topic for future work; here, we only claim that the rapid changes in GIC seen near the time of the density pulse originate from the density pulse, whether directly or indirectly via an intermediate current system/wave that was excited by the density pulse.

There is value in comparing GIC observations between sites, especially when they are referenced to past geomagnetic storms and/or long-term monitoring intervals. Indeed, this is one of the approaches used to understand what types of GMD generally lead to the largest amplitude GIC and expected power system impacts at different magnetic latitudes and local times (Clilverd et al., 2021; Kappenman, 2003) and to assess for a given type of event where power system impacts might be expected since GIC measurements are the quantity most closely associated with power system performance (Pulkkinen et al., 2017). However, it is important to recognize that simply comparing GIC values across different sites in a given event may not provide meaningful insights without additional contextual information, such as reference values to past monitoring intervals at each site. This is because GIC levels for a given GMD are influenced by the interplay between multiple factors including the specific configurations of power systems and the underlying conductivity structure of the Earth. For example, GIC recordings in a natural gas pipeline (e.g., top panel of Figure 9) would likely exhibit significant differences from those in a power grid. Although the fundamental physics might remain the same, the grounding setup differs substantially between the two—while a power grid is earthed only at transformer grounding points, a gas network remains almost continuously earthed. Moreover, the magnitude of GIC heavily depends on factors such as the electrical resistance of the network elements (e.g., transmission lines and transformer windings), the layout of the grounded systems, and the conductivity of the Earth itself, all of which vary widely across different networks, such as power grids in the US, Canada, and Finnish pipelines. Finally, there is an interplay between the event-specific geoelectric field properties and power system properties that further determines GIC amplitude for a given power system in a given event, for example, relative orientation of the event-specific geoelectric field and power lines in the network (Cordell et al., 2024).

We address the above concerns by focusing on comparing GIC measurements at different sites after referencing them to past monitoring intervals, or at least a set of past geomagnetic storm events. This allows us to more quantitatively demonstrate that this type of CME density pulse can drive GIC comparable to other more firmly established sources of GIC that occurred during these monitoring intervals (e.g., interplanetary shocks), thus assess whether this type of density pulse should be considered an important driver of GIC; this type of analysis provides valuable additional insight when compared to, for example, past studies that relied exclusively on GMD

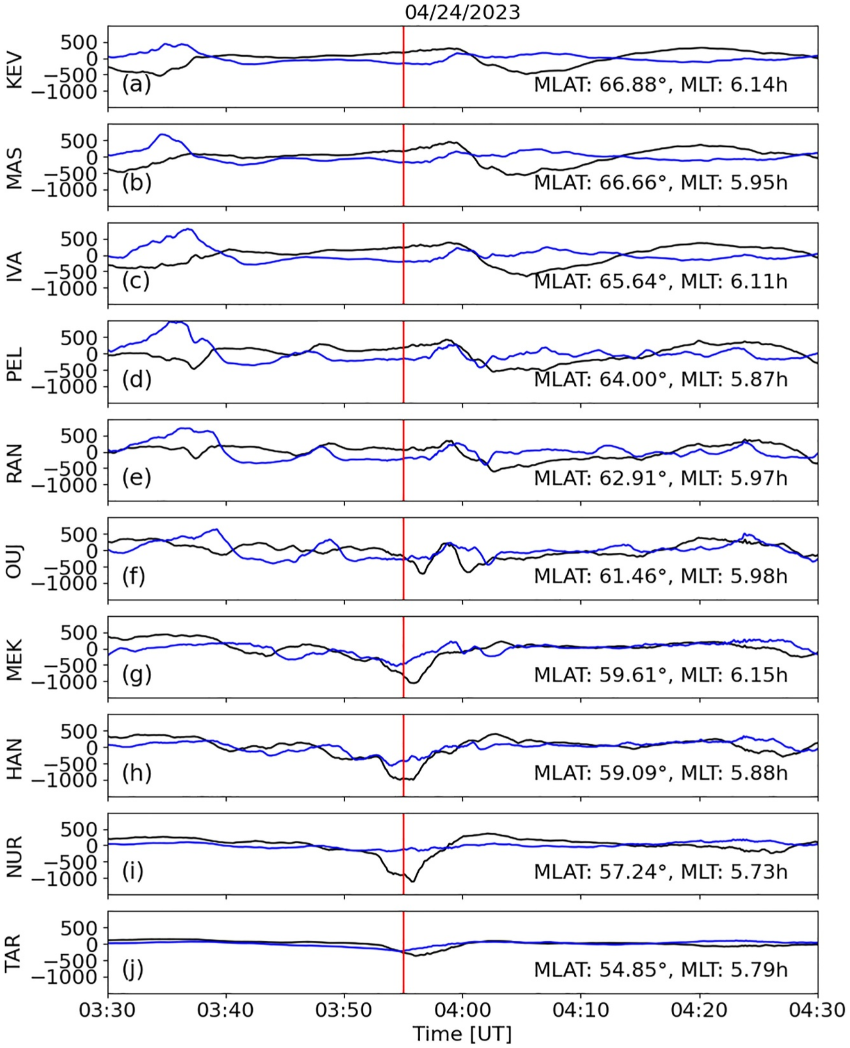

Figure 7. Ground magnetic field perturbations in the northward (black: ΔB_x) and eastward (blue: ΔB_y) component from a latitudinal ground magnetometer chain from the Finnish Meteorological Institute array around dawn. The vertical red line marks 03:55 UT.

measurements to estimate GIC amplitudes or studies that used GIC measurements from a single location. Table 1 shows the maximum values reported at each of the sites shown in Figure 9 compared against reference values from long monitoring intervals or recent geomagnetic storms of comparable magnitude. From this, we can see that measurements from both NERC GMD devices reported their largest GIC during the time interval shown in Figure 9. This includes the value of 58.1 A reported by NERC Device 10659 (Figure 9c), which was the largest measured over a 2-year interval from November 2021–January 2024 (Figure S6 in Supporting Information S1). At other mid-latitude locations, the measured GIC were large but smaller than maximum values reported over extended monitoring intervals, ranging from ~21%–62% of peak values. These results suggest that the density pulses embedded in CME should be considered an important driver of GIC, at least relative to other disturbances that occurred during the extended monitoring intervals and $Kp \geq 7$ geomagnetic storm events listed in Table 1, including GMD related to other types of density pulses such as those associated with interplanetary shocks.

It is perhaps not surprising that the maximum GIC in this study from the New Zealand site (16 A) is only half of the GIC amplitude in 14-year maximum (34.1 A). In this study when the solar wind density pulses arrived, the New Zealand ISL site was located in the afternoon sector (red diamond in Figure 6), while the largest geomagnetic perturbations were observed from the pre-midnight to the dawn sector (Figure 8). The geomagnetic perturbations from a nearby ground magnetometer site (EYR, shown in Figure S5 in Supporting Information S1) are large but

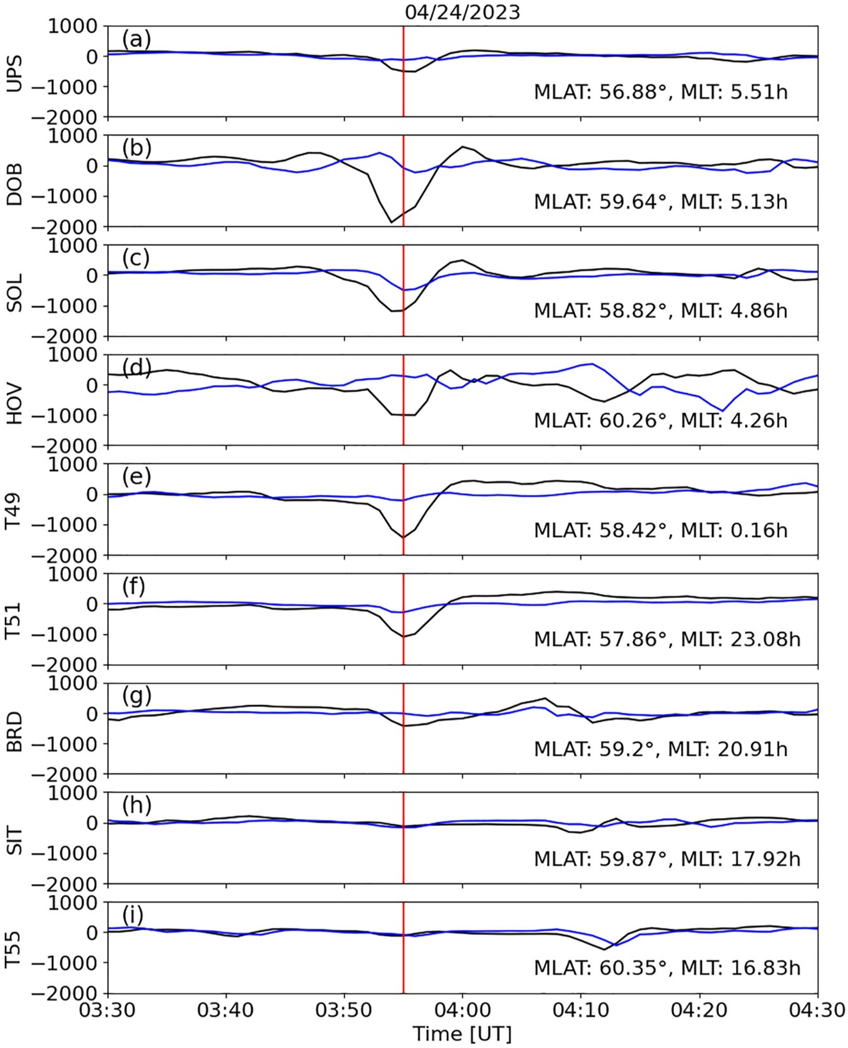

Figure 8. Ground magnetic field perturbations in the northward (black: ΔB_x) and eastward (blue: ΔB_y) component from a longitudinal ground magnetometer chain at 57–60° MLAT from SuperMAG. The vertical red line marks 03:55 UT.

not exceptionally large, with maximum perturbations up to ∼100 nT in ΔB and ∼3 nT/s in dH/dt from 1-s sampling rate data.

In the location where significant geomagnetic perturbations were observed around dawn (∼1,000 nT in ΔB and ∼18 nT/s in dH/dt from 1-s sampling rate NUR ground magnetometer data shown in Figure S5 in Supporting Information S1), large GIC were observed from the Finland gas pipeline in this study with maximum amplitude of ∼35 A at 03:56:40 UT (note the FMI GIC fluctuations after about 04:10 UT is due to noise). It is comparable to but does not exceed the 25-year maximum value of 57 A (Table 1) which was produced during the 2003 Halloween storm (Dimmock et al., 2019; Tsurutani & Hajra, 2021; Viljanen et al., 2010). The FMI GIC site is located at relatively higher latitudes (57.35° MLAT) compared to other GIC sites used in this study, thus high latitude auroral electrojets during substorms or the main phase of storms may play a more important role driving GIC there. Despirak et al. (2023) also examined GIC during this storm in a power grid at a still higher latitude location but similar local time region: the Kola Peninsula in Russia. At the Vykhodnoy (VKH) site located at MLAT of 65.53°, they find a maximum GIC of ∼45 A during the storm, at the same time as the peak GIC was observed in the present study (∼0350–0400 UT) and is associated with "local substorm-like intensification with intense pulsations" (Despirak et al., 2023), in other words the same electrojet structure indicated in Figure 7 (see Figure 6 of Despirak et al. (2023) for a comparable plot). For context, this GIC is notable but it is not the largest GIC ever reported at VKH; for example, Apatenkov et al. (2020) found GIC of ∼120–140 A during an auroral omega band event (though we do not know if there were any changes to the Kola power grid between the two measurements). A similar scenario also applies to the Alberta GIC observations at similar magnetic latitudes as the FMI GIC site, although the geomagnetic perturbations were much weaker in Alberta compared to Finland (Figure S5 in Supporting Information S1). Note that some GIC measurements have inherent errors and may be susceptible to drift (Cordell et al., 2024). In particular, the Alberta sensor has an inconsistent sample rate resulting in gaps in the time series which are linearly interpolated, for example, the temporal resolution before 04:08 UT is lower than those after as can be seen in Figure 9e.

Figure 9 panels b and c show perhaps the most surprising results in this study: this solar wind density pulse led to intense GIC at low- and mid-latitude locations. In particular, for both NERC sites (NB Power and ATC in Table 1), the maximum GIC in this study is the maximum value in the NERC GMD database with four $Kp \geq 7$ storms in 2022–2023 for the NB Power device and two $Kp \geq 7$ storms in 2023 for the ATC device. ATC also provided a GIC plot (Figure S6 in Supporting Information S1) for a two year interval from November 2021 to January 2024 confirming that the reported maximum GIC of 58.1 A for this site is the largest in the past two years. Note that the reference values for the NERC sites are derived from storms with $Kp \geq 7$ in 2022–2023. These reference periods are relatively short compared to the 14-year period for New Zealand and the 25-year period for Finland, with the latter including information from stronger storms, such as the 2003 Halloween storm, which generated the maximum GIC value (57 A) for a 25-year period in the Finnish gas pipeline.

Finally, several panels of Figure 9 show wave-like GIC variations that may be related to ULF waves that have a range of periods, from ~5–10 min (e.g., panel b) to ~1 min (e.g., panel c), the latter occurring during the period with the 58.1 A maximum GIC. As noted in recent studies, many of these wave-like GIC variations would have been undersampled or removed if the GIC measurements had been collected with 1 min sampling intervals (Hartinger et al., 2023; Trichtchenko, 2021). Moreover, they would also have been easily missed in visual inspection of GMD plots that tend to emphasize the larger, slow varying disturbances that may not always contribute significantly to GIC (e.g., compare panels e and g of Figure 5, especially from 0405 to 0415 UT). More work is needed to determine the source of these wave-like variations, including possible connections with magnetospheric ULF waves.

4. Discussion and Conclusions

In this study, we use a range of satellite and ground-based measurements to identify the upstream driver of global GMD and GIC during the 23–24 April 2023 geomagnetic storm, focusing on one particular time interval with significant GIC observed at many locations (see Table 1).

In particular, we identify a global-scale density pulse with field geometry similar to a magnetic bottle mainly in the GSE-YZ plane, associated with a CME event. It was a pressure-balanced structure, and due to the very low plasma β, a very slight field strength depletion caused an extremely intense density enhancement, leading to significant dynamic pressure enhancement. As a result, when the structure encountered the bow shock, the entire bow shock moved inward by more than 6 R_E and the magnetopause moved inward by 1.3–2 R_E over ~10–20 min. Due to this extremely large magnetopause disturbance, ground magnetic field perturbations of ~1,000–2,000 nT were observed at ~ 60° MLAT from midnight to dawnside in the northern hemisphere. At the same time interval, GIC measured in New Zealand, Finland, Canada, and the United States were observed comparable (within factors of 2–2.5) to the largest ever recorded during ≥14 year monitoring intervals in New Zealand and Finland and represented ~2-year maxima in the United States during a period with several Kp ≥ 7 geomagnetic storms.

Pressure-balanced structures have been commonly observed across the heliosphere which can frequently reach the Earth. When they are embedded in some extreme plasma conditions like those which occur around CMEs, they can become extreme intense density/dynamic pressure pulses, leading to significant back-and-forth motion of the bow shock and magnetopause. This indicates that during magnetic storms, there are not only long-time scale disturbances driven by the CMEs but also some structures on the scale of 10 min with very significant amplitudes, which could cause unexpected space weather hazards. Such structures last long enough for the magnetosphere and ionosphere to respond but also provide sufficiently sharp time variation to generate large geoelectric fields and GIC. For example, Lugaz et al. (2015) observed an interplanetary shock (driven by an overtaking CIR) embedded in a CME. The combined effects of sudden dynamic pressure increase by the interplanetary shock and strong southward IMF within the CME lead to intense GMD, even though the CME itself

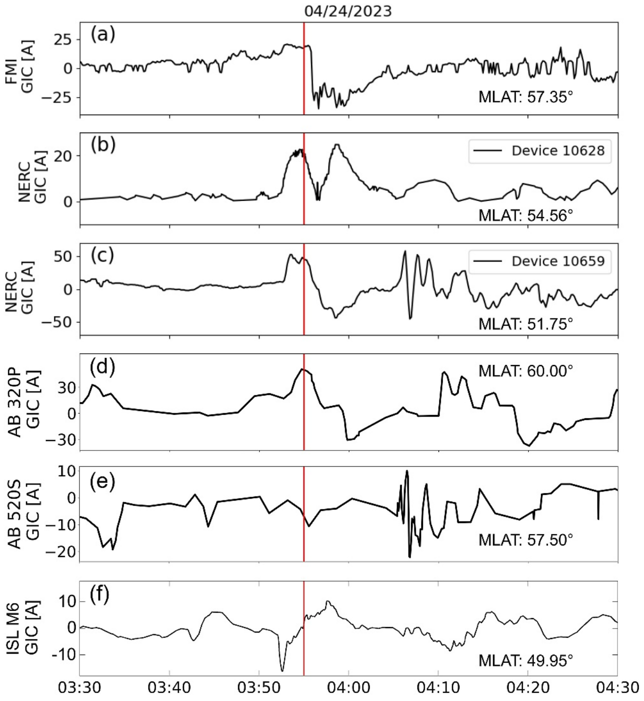

Figure 9. Geomagnetically induced currents measurements from multiple sites across the world including (a) Finland (Finnish natural gas pipeline, MLAT: 57.35°), (b) Canada (power grid, NERC device 10628, MLAT: 54.56°), (c) United States (power grid, NERC device 10659, MLAT: 51.75°), (d) Canada (power grid, 320P, MLAT: 60.00°), (e) Canada (power grid, 520S, MLAT: 57.5°), and (f) New Zealand (power grid, ISL-M6 site, MLAT: -49.95°). The vertical red line marks 03:55 UT.

is rather weak. In the future, a statistical survey is needed to examine the occurrence rate of such significant transient-scale density pulses and further investigate their impacts.

The density pulse and related magnetopause disturbance caused magnetosphere-ionosphere currents (Sibeck, 1990), and these currents in turn led to global scale GMD as well as GIC at several locations. Most studies of GMD do not include simultaneous GIC measurements, or if they do have GIC measurements they are taken from a single power system/power grid. In this study, we compare GIC measurements from multiple power systems distributed around the world, each compared to reference values unique to each system. This allowed us to show that a particular solar wind transient generated significant GIC at many widely separated locations. Although the GIC did not lead to any power system disruptions, the values measured were among the largest, or were the largest, ever reported during extended monitoring intervals at several locations. Thus, to the extent that any source of GIC in these power systems (Table 1) can be considered significant, these density pulses should be considered significant. It is also worth noting that GIC values reported for this event (Table 1) approach the thresholds of 75 A (benchmark event) and 85 A (supplemental event) required for a transformer thermal impact assessment based on the NERC TPL-007-4 reliability standard (North American Electric Reliability Corporation, 2020). While this event did not produce significant power system impacts, it is also not among the largest geomagnetic storms ever reported; it is plausible that future CME density pulses could lead to GIC that exceed these thresholds, especially since we have limited historic solar wind measurements available to assess the types of density pulses that might have occurred during historic geomagnetic storms that produced known power system impacts.

In this study, we reported GIC measurements from five different power systems at a wide range of magnetic latitudes and longitudes (Table 1, Figure 9). This allows us to glean important insights not typically discussed in past studies, as GIC measurements are rarely available at multiple locations for the same event. Although previous studies have acknowledged that GICs depend on various factors, including the spatial and temporal variability of GMDs, local ground conductivity, and power system configuration, the wide range of potential responses for the same event is seldom examined or reported likely due to the scarcity of multi-point GIC measurements. Therefore, comparisons between sites as shown in Figure 9 and Table 1 offer important new insights into the diverse responses observed in different locations, in addition to demonstrating that density pulses embedded in CME can drive significant amplitude GIC (previous paragraph).

Although the density pulse produced GMD globally, there was significant regional variability concerning amplitude and frequency content, likely due to various M-I current systems and waves driven by the density pulse. At the dawnside and nightside, where intense GICs were observed at FMI, NERC, Alberta sites, our analysis suggests a driver related to the westward ionospheric auroral electrojet. This is due to enhanced ionospheric conductivity caused by diffuse precipitation, as suggested by Zou et al. (2024), who conducted a detailed analysis using magnetospheric and ionospheric measurements (e.g., GOES, AMPERE, Swarm, and TREx auroral camera). For the New Zealand site located at about −50° MLAT in the afternoon sector, the potential driver could be an enhanced magnetopause current due to the compression effects of the density pulse. The magnetic field perturbations from the EYR site (near the NZ Power Grid Transformer ISL M6) show similar signatures to those in the dayside low-latitude regions due to the magnetopause current (see Figure S7 in Supporting Information S1). Additionally, ULF waves, also known as geomagnetic pulsations, are usually generated following solar wind density pulses or during magnetic storms, as reported by many previous studies (Ngwira et al., 2018; Oliveira et al., 2021), and may be related to the wave-like GIC signatures shown in Figure 9. For example, at the ATC transformer where the largest GIC were reported, wave-like structures with periods of ~1 min were observed during the period with maximum GIC (58.1 A). These GIC variations are similar to other large amplitude GIC events reported in the continental USA and in other mid-latitude locations (Hartinger et al., 2023; Heyns et al., 2021; Kappenman, 2003; Oyedokun et al., 2020). They highlight the need to better understand how these variations are produced, particularly since power system modeling work suggests that high-frequency GICs $(\sim 4 - 25 mHz)$, whether from pulsations or impulses, may be more of a concern for power system voltage stability than lower frequency components (Jankee et al., 2022). In general, more work is needed to understand how density pulses generate GMD and ultimately GIC in comparison (and contrast) to other sources of solar wind density and pressure variations and other mechanisms that lead to nightside GMD/GIC. This work also highlights the need to collect GMD and GIC measurements at uniform, 1s sampling intervals (Trichtchenko, 2021).

Acknowledgments
XS is supported by NASA awards 80NSSC24K1026, 80NSSC19K0907, 80NSSC21K1677, NSF award AGS-1935110, and by the NASA DRIVE Science Center for Geospace Storms (CGS) under award 80NSSC22M0163. MH is supported by NASA award 80NSSC19K0907 and NSF awards AGS-2027210 and AGS-2307204. TL is supported by NASA award 80NSSC23K0903 and 80NSSC23K0086. We acknowledge support by the NASA THEMIS contract NAS5-02099. HM was supported by NASA Grant 80NSSC23K0009. CJR and DHM acknowledge support by New Zealand Ministry of Business, Innovation & Employment Hazards and Infrastructure Research Fund Contract UOOX2002. We thank K. H. Glassmeier, U. Auster, and W. Baumjohann for the use of the THEMIS/FGM data provided under the lead of the Technical University of Braunschweig and with financial support through the German Ministry for Economy and Technology and the German Center for Aviation and Space (DLR) under contract 50 OC 0302. We also thank the late C. W. Carlson and J. P. McFadden for use of THEMIS/ESA data. We also thank the SPEDAS team and the NASA Coordinated Data Analysis Web. TL acknowledges discussion with ISSI team led by Primoz Kajdic. For the ground magnetometer data we gratefully acknowledge: IMAGE, PI Liisa Juusola; Finnish Meteorological Institute, PI Liisa Juusola; MagStar, PI Jennifer Gannon; SuperMAG, PI Jesper W. Gjerloev; CARISMA, PI Ian Mann. FMI GIC recordings were maintained by the Finnish Meteorological Institute, supported by Gasum Oy until December 2010. In March 2011 to February 2014, maintenance of the recordings received funding from the European Community's Seventh Framework Programme (FP7/2007–2013) under grant agreement no 260330 (EURISGIC). We thank American Transmission Company, LLC for valuable insights into Device 10659 GIC measurements as well as for providing the corresponding 2-year GIC plot in Supporting Information S1 (Figure S6). We dedicate this study to the memory of Dr. Jennifer Gannon, who was a leader in the GIC, GMD, and broader space weather research communities (https://agupubs.onlinelibrary.wiley.com/doi/full/10.1029/2024SW004016). Gannon provided the MagStar magnetometer measurements used in this study and valuable insights into the data quality.

Space weather models are increasingly being used to provide nowcasts and forecasts of geomagnetic activity, GMD, and geoelectric fields (e.g., Kelbert et al., 2017; Malone-Leigh et al., 2023). This work suggests that such models should be able to capture density pulses in the solar wind, not just the interplanetary shocks most often discussed in conjunction with GMD and GIC. Different modeling techniques may be necessary compared to those required for modeling density pulses linked to locally formed foreshock transient phenomena or fluctuations in the solar wind associated with Alfvén waves. Some large scale density pulses may form close to the Sun and evolve relatively slowly as they move toward the Earth, potentially making it possible to provide useable predictions further in advance. More work is needed to explore what factors (simulation grid resolution, boundary condition, etc.) are needed to model the development, evolution, and magnetosphere-ionosphere impacts of these structures.

Data Availability Statement

THEMIS, MMS, and DSCOVR dataset are available at NASA's Coordinated Data Analysis Web (CDAWeb, http://cdaweb.gsfc.nasa.gov/). KOMPSAT dataset is available at https://swe.ssa.esa.int/sosmag. The SPEDAS software (see Angelopoulos et al., 2019) is available at http://themis.ssl.berkeley.edu. 1-s resolution FMI ground magnetometer data are available at: https://space.fmi.fi/image/plasmon/. FMI GIC recording are at: https://space.fmi.fi/gic/index.php?page=gasum_final. MAGStar site HET ground magnetometer are at: http://cedar.openmadrigal.org/. SuperMAG data are available at: https://supermag.jhuapl.edu/info/. North American Electric Reliability Corporation Geomagnetic Disturbance Database last accessed on 5 January 2024 at: https://eroportal.nerc.net/gmd-data-home/. Following the confidentiality restriction on data use, the GIC network and transformer details and exact location are not provided in this paper. The New Zealand LEM DC and harmonic distortion data were provided to us by Transpower New Zealand with caveats and restrictions. This includes requirements of permission before all publications and presentations. In addition, we are unable to directly provide the New Zealand LEM DC data or derived GIC observations. Requests for access to the measurements need to be made to Transpower New Zealand. At this time the contact point is Michael Dalzell (Michael.Dalzell@transpower.co.nz).

References

Ala-Lahti, M. M., Kilpua, E. K. J., Dimmock, A. P., Osmane, A., Pulkkinen, T., & Souček, J. (2018). Statistical analysis of mirror mode waves in sheath regions driven by interplanetary coronal mass ejection. *Annales Geophysicae*, *36*(3), 793–808. https://doi.org/10.5194/angeo-36-793-2018

Angelopoulos, V. (2008). The THEMIS mission. *Space Science Reviews*, *141*(1), 5–34. https://doi.org/10.1007/s11214-008-9336-1

Angelopoulos, V., Cruce, P., Drozdov, A., Grimes, E. W., Hatzigeorgiu, N., King, D. A., et al. (2019). The space physics environment data analysis system (SPEDAS) [Software]. *Space Science Reviews*, *215*(1), 9. https://doi.org/10.1007/s11214-018-0576-4

Apatenkov, S. V., Pilipenko, V. A., Gordeev, E. I., Viljanen, A., Juusola, L., Belakhovsky, V. B., et al. (2020). Auroral Omega bands are a significant cause of large geomagnetically induced currents. *Geophysical Research Letters*, *47*(6), e86677. https://doi.org/10.1029/2019GL086677

Araki, T. (1994). A physical model of the geomagnetic sudden commencement. *Geophysical Monograph-American Geophysical Union*, *81*, 183–200. https://doi.org/10.1029/gm081p0183

Auster, H. U., Glassmeier, K. H., Magnes, W., Aydogar, O., Baumjohann, W., Constantinescu, D., et al. (2008). The THEMIS fluxgate magnetometer. *Space Science Reviews*, *141*(1), 235–264. https://doi.org/10.1007/s11214-008-9365-9

Boteler, D. H. (2019). A 21st century view of the March 1989 magnetic storm. *Space Weather*, *17*(10), 1427–1441. https://doi.org/10.1029/2019SW002278

Burch, J. L., Moore, T. E., Torbert, R. B., & Giles, B. L. (2016). Magnetospheric multiscale overview and science objectives. *Space Science Reviews*, *199*(1), 5–21. https://doi.org/10.1007/s11214-015-0164-9

Chandrasekhar, S., Kaufman, A. N., & Watson, K. M. (1958). The stability of the pinch. *Proceedings of the Royal Society of London*, *245*(1243), 435–455.

Clilverd, M. A., Rodger, C. J., Brundell, J. B., Dalzell, M., Martin, I., Mac Manus, D. H., & Thomson, N. R. (2020). Geomagnetically induced currents and harmonic distortion: High time resolution case studies. *Space Weather*, *18*(10), e02594. https://doi.org/10.1029/2020SW002594

Clilverd, M. A., Rodger, C. J., Freeman, M. P., Brundell, J. B., Manus, M., Daniel, H., et al. (2021). Geomagnetically induced currents during the 07–08 September 2017 disturbed period: A global perspective. *Journal of Space Weather and Space Climate*, *11*, 33. https://doi.org/10.1051/swsc/2021014

Cordell, D., Mann, I. R., Parry, H., Unsworth, M. J., Cui, R., Clark, C., et al. (2024). Modeling geomagnetically induced currents in the Alberta power network: Comparison and validation using hall probe measurements during a magnetic storm. *Space Weather*, *22*(4), e2023SW003813. https://doi.org/10.1029/2023SW003813

Cordell, D., Unsworth, M. J., Lee, B., Hanneson, C., Milling, D. K., & Mann, I. R. (2021). Estimating the geoelectric field and electric power transmission line voltage during a geomagnetic storm in Alberta, Canada using measured magnetotelluric impedance data: The influence of three-dimensional electrical structures in the lithosphere. *Space Weather*, *19*(10), e2021SW002803. https://doi.org/10.1029/2021SW002803

Despirak, I., Setsko, P., Lubchich, A., Hajra, R., Sakharov, Y., Lakhina, G., et al. (2023). Geomagnetically induced currents (GICS) during strong geomagnetic activity (storms, substorms, and magnetic pulsations) on 23–24 April 2023.

Dimmock, A. P., Osmane, A., Pulkkinen, T. I., & Nykyri, K. (2015). A statistical study of the dawn-dusk asymmetry of ion temperature anisotropy and mirror mode occurrence in the terrestrial dayside magnetosheath using THEMIS data. *Journal of Geophysical Research: Space Physics*, *120*(7), 5489–5503. https://doi.org/10.1002/2015JA021192

Dimmock, A. P., Rosenqvist, L., Hall, J.-O., Viljanen, A., Yordanova, E., Honkonen, I., et al. (2019). The gic and geomagnetic response over fennoscandia to the 7–8 September 2017 geomagnetic storm. *Space Weather*, *17*(7), 989–1010. https://doi.org/10.1029/2018SW002132

Dimmock, A. P., Yordanova, E., Graham, D. B., Khotyaintsev, Y. V., Blanco-Cano, X., Kajdič, P., et al. (2022). Mirror mode storms observed by solar orbiter. *Journal of Geophysical Research: Space Physics*, *127*(11), e2022JA030754. https://doi.org/10.1029/2022JA030754

Espinosa, K. V., Padilha, A. L., & Alves, L. R. (2019). Effects of ionospheric conductivity and ground conductance on geomagnetically induced currents during geomagnetic storms: Case studies at low-latitude and equatorial regions. *Space Weather*, *17*(2), 252–268. https://doi.org/10.1029/2018SW002094

Fiori, R. A. D., Boteler, D. H., & Gillies, D. M. (2014). Assessment of gic risk due to geomagnetic sudden commencements and identification of the current systems responsible. *Space Weather*, *12*(1), 76–91. https://doi.org/10.1002/2013SW000967

Gannon, J. (2023). Computational physics. (2023) magstar data from the cedar madrigal database.

Ghag, K., Raghav, A., Bhaskar, A., Soni, S. L., Sathe, B., Shaikh, Z., et al. (2024). Quasi-planar ICME sheath: A cause of the first two-step extreme geomagnetic storm of the 25th solar cycle observed on 23 April 2023. *Advances in Space Research*, *73*(12), 6288–6297. https://doi.org/10.1016/j.asr.2024.03.011

Gjerloev, J. W. (2012). The SuperMAG data processing technique. *Journal of Geophysical Research*, *117*(A9), A09213. https://doi.org/10.1029/2012JA017683

Gonzalez, W. D., Joselyn, J. A., Kamide, Y., Kroehl, H. W., Rostoker, G., Tsurutani, B. T., & Vasyliunas, V. M. (1994). What is a geomagnetic storm? *Journal of Geophysical Research*, *99*(A4), 5771–5792. https://doi.org/10.1029/93JA02867

Hartinger, M. D., Shi, X., Rodger, C. J., Fujii, I., Rigler, E. J., Kappler, K., et al. (2023). Determining ULF wave contributions to geomagnetically induced currents: The important role of sampling rate. *Space Weather*, *21*(5), e2022SW003340. https://doi.org/10.1029/2022SW003340

Hasegawa, A. (1969). Drift mirror instability in the magnetosphere. *The Physics of Fluids*, *12*(12), 2642–2650. https://doi.org/10.1063/1.1692407

He, J., Tu, C., Marsch, E., Chen, C. H. K., Wang, L., Pei, Z., et al. (2015). Proton heating in solar wind compressible turbulence with collisions between counter-propagating waves. *The Astrophysical Journal Letters*, *813*(2), L30. https://doi.org/10.1088/2041-8205/813/2/l30

Heyns, M. J., Lotz, S. I., & Gaunt, C. T. (2021). Geomagnetic pulsations driving geomagnetically induced currents. *Space Weather*, *19*(2), e02557. https://doi.org/10.1029/2020SW002557

Howes, G. G., Bale, S. D., Klein, K. G., Chen, C. H. K., Salem, C. S., & TenBarge, J. M. (2012). The slow-mode nature of compressible wave power in solar wind turbulence. *The Astrophysical Journal Letters*, *753*(1), L19. https://doi.org/10.1088/2041-8205/753/1/l19

Jankee, P., Oyedokun, D., Soltanian, M., Chisepo, H. K., & Heyns, M. (2022). Geomagnetically induced currents: Frequency spectra and threats to voltage stability. *IEEE Access*, *10*, 62484–62501. https://doi.org/10.1109/ACCESS.2022.3182237

Juusola, L., Viljanen, A., Dimmock, A. P., Kellinsalmi, M., Schillings, A., & Weygand, J. M. (2023). Drivers of rapid geomagnetic variations at high latitudes. *Annales Geophysicae*, *41*(1), 13–37. https://doi.org/10.5194/angeo-41-13-2023

Kappenman, J. G. (2003). Storm sudden commencement events and the associated geomagnetically induced current risks to ground-based systems at low-latitude and midlatitude locations. *Space Weather*, *1*(3), 1016. https://doi.org/10.1029/2003SW000009

Kelbert, A., Balch, C. C., Pulkkinen, A., Egbert, G. D., Love, J. J., Rigler, E. J., & Fujii, I. (2017). Methodology for time-domain estimation of storm time geoelectric fields using the 3-D magnetotelluric response tensors. *Space Weather*, *15*(7), 874–894. https://doi.org/10.1002/2017SW001594

Kilpua, E. K. J., Fontaine, D., Moissard, C., Ala-Lahti, M., Palmerio, E., Yordanova, E., et al. (2019). Solar wind properties and Geospace impact of coronal mass ejection-driven sheath regions: Variation and driver dependence. *Space Weather*, *17*(8), 1257–1280. https://doi.org/10.1029/2019SW002217

Kim, B. K. (1999). An overview of the Korea multi-purpose satellite (KOMPSAT). In F.-B. Hsiao (Ed.), *Microsatellites as research tools* (Vol. 10, pp. 66–73). Pergamon. https://doi.org/10.1016/S0964-2749(99)80010-9

Loto'aniu, P. T. M., Romich, K., Rowland, W., Codrescu, S., Biesecker, D., Johnson, J., et al. (2022). Validation of the DSCOVR spacecraft mission space weather solar wind products. *Space Weather*, *20*(10), e2022SW003085. https://doi.org/10.1029/2022SW003085

Love, J. J., Lucas, G. M., Bedrosian, P. A., & Kelbert, A. (2019). Extreme-value geoelectric amplitude and polarization across the Northeast United States. *Space Weather*, *17*(3), 379–395. https://doi.org/10.1029/2018SW002068

Love, J. J., Lucas, G. M., Kelbert, A., & Bedrosian, P. A. (2018). Geoelectric hazard maps for the mid-atlantic United States: 100 year extreme values and the 1989 magnetic storm. *Geophysical Research Letters*, *45*(1), 5–14. https://doi.org/10.1002/2017GL076042

Love, J. J., Lucas, G. M., Rigler, E. J., Murphy, B. S., Kelbert, A., & Bedrosian, P. A. (2022). Mapping a magnetic superstorm: March 1989 geoelectric hazards and impacts on United States power systems. *Space Weather*, *20*(5), e2021SW003030. https://doi.org/10.1029/2021SW003030

Love, J. J., Rigler, E. J., Hartinger, M. D., Lucas, G. M., Kelbert, A., & Bedrosian, P. A. (2023). The March 1940 superstorm: Geoelectromagnetic hazards and impacts on American communication and power systems. *Space Weather*, *21*(6), e2022SW003379. https://doi.org/10.1029/2022SW003379

Lucas, G. M., Love, J. J., Kelbert, A., Bedrosian, P. A., & Rigler, E. J. (2020). A 100-year geoelectric hazard analysis for the U.S. High-voltage power grid. *Space Weather*, *18*(2), e02329. https://doi.org/10.1029/2019SW002329

Lugaz, N., Farrugia, C. J., Huang, C.-L., & Spence, H. E. (2015). Extreme geomagnetic disturbances due to shocks within CMES. *Geophysical Research Letters*, *42*(12), 4694–4701. https://doi.org/10.1002/2015GL064530

Mac Manus, D. H., Rodger, C. J., Dalzell, M., Thomson, A. W., Clilverd, M. A., Petersen, T., et al. (2017). Long-term geomagnetically induced current observations in New Zealand: Earth return corrections and geomagnetic field driver. *Space Weather*, *15*(8), 1020–1038. https://doi.org/10.1002/2017SW001635

Magnes, W., Hillenmaier, O., Auster, H. U., Brown, P., Kraft, S., Seon, J., et al. (2020). Space weather magnetometer aboard GEO-KOMPSAT-2A. *Space Science Reviews*, *216*(8), 119. https://doi.org/10.1007/s11214-020-00742-2

Malone-Leigh, J., Campanyà, J., Gallagher, P. T., Neukirch, M., Hogg, C., & Hodgson, J. (2023). Nowcasting geoelectric fields in Ireland using magnetotelluric transfer functions. *Journal of Space Weather and Space Climate*, *13*, 6. https://doi.org/10.1051/swsc/2023004

Marin, J., Pilipenko, V., Kozyreva, O., Stepanova, M., Engebretson, M., Vega, P., & Zesta, E. (2014). Global Pc5 pulsations during strong magnetic storms: Excitation mechanisms and equatorward expansion. *Annales Geophysicae*, *32*(4), 319–331. https://doi.org/10.5194/angeo-32-319-2014

McFadden, J. P., Carlson, C. W., Larson, D., Ludlam, M., Abiad, R., Elliott, B., et al. (2008). The THEMIS ESA plasma instrument and in-flight calibration. *Space Science Reviews*, *141*(1), 277–302. https://doi.org/10.1007/s11214-008-9440-2

Merka, J., Szabo, A., Slavin, J. A., & Peredo, M. (2005). Three-dimensional position and shape of the bow shock and their variation with upstream mach numbers and interplanetary magnetic field orientation. *Journal of Geophysical Research*, *110*(A4), 47. https://doi.org/10.1029/2004JA010944

Narita, Y., & Marsch, E. (2015). Kinetic slow mode in the solar wind and its possible role in turbulence dissipation and ion heating. *The Astrophysical Journal*, *805*(1), 24. https://doi.org/10.1088/0004-637x/805/1/24

Ngwira, C. M., Sibeck, D., Silveira, M. V. D., Georgiou, M., Weygand, J. M., Nishimura, Y., & Hampton, D. (2018). A study of intense local db/dt variations during two geomagnetic storms. *Space Weather*, *16*(6), 676–693. https://doi.org/10.1029/2018SW001911

North American Electric Reliability Corporation. (2020). TPL-007-4—Transmission system planned performance for geomagnetic disturbance events.

Oliveira, D. M., Weygand, J. M., Zesta, E., Ngwira, C. M., Hartinger, M. D., Xu, Z., et al. (2021). Impact angle control of local intense db/dt variations during shock-induced substorms. *Space Weather*, *19*(12), e2021SW002933. https://doi.org/10.1029/2021SW002933

Oliveira, D. M., Zesta, E., & Vidal-Luengo, S. (2024). First direct observations of interplanetary shock impact angle effects on actual geomagnetically induced currents: The case of the Finnish natural gas pipeline system. *Frontiers in Astronomy and Space Sciences*, *11*, 29. https://doi.org/10.3389/fspas.2024.1392697

Oyedokun, D., Heyns, M., Cilliers, P., & Gaunt, C. (2020). Frequency components of geomagnetically induced currents for power system modelling. In *2020 international SAUPEC/RobMech/PRASA conference* (pp. 1–6). https://doi.org/10.1109/SAUPEC/RobMech/PRASA48453.2020.9041021

Patterson, C. J., Wild, J. A., & Boteler, D. H. (2023). Modeling the impact of geomagnetically induced currents on electrified railway signaling systems in the United Kingdom. *Space Weather*, *21*(3), e2022SW003385. https://doi.org/10.1029/2022SW003385

Pilipenko, V. (2021). Space weather impact on ground-based technological systems. *Solar-Terrestrial Physics*, *7*(3), 68–104. https://doi.org/10.12737/stp-73202106

Pollock, C., Moore, T., Jacques, A., Burch, J., Gliese, U., Saito, Y., et al. (2016). Fast plasma investigation for magnetospheric multiscale. *Space Science Reviews*, *199*(1), 331–406. https://doi.org/10.1007/s11214-016-0245-4

Pulkkinen, A., Bernabeu, E., Thomson, A., Viljanen, A., Pirjola, R., Boteler, D., et al. (2017). Geomagnetically induced currents: Science, engineering, and applications readiness. *Space Weather*, *15*(7), 828–856. https://doi.org/10.1002/2016SW001501

Pulkkinen, A., Lindahl, S., Viljanen, A., & Pirjola, R. (2005). Geomagnetic storm of 29–31 October 2003: Geomagnetically induced currents and their relation to problems in the Swedish high-voltage power transmission system. *Space Weather*, *3*(8), S08C03. https://doi.org/10.1029/2004SW000123

Rodger, C. J., Clilverd, M. A., Mac Manus, D. H., Martin, I., Dalzell, M., Brundell, J. B., et al. (2020). Geomagnetically induced currents and harmonic distortion: Storm-time observations from New Zealand. *Space Weather*, *18*(3), e02387. https://doi.org/10.1029/2019SW002387

Rodger, C. J., Mac Manus, D. H., Dalzell, M., Thomson, A. W. P., Clarke, E., Petersen, T., et al. (2017). Long-term geomagnetically induced current observations from New Zealand: Peak current estimates for extreme geomagnetic storms. *Space Weather*, *15*(11), 1447–1460. https://doi.org/10.1002/2017SW001691

Russell, C. T., Anderson, B. J., Baumjohann, W., Bromund, K. R., Dearborn, D., Fischer, D., et al. (2016). The magnetospheric multiscale magnetometers. *Space Science Reviews*, *199*(1), 189–256. https://doi.org/10.1007/s11214-014-0057-3

Schillings, A., Palin, L., Opgenoorth, H. J., Hamrin, M., Rosenqvist, L., Gjerloev, J. W., et al. (2022). Distribution and occurrence frequency of db/dt spikes during magnetic storms 1980–2020. *Space Weather*, *20*(5), e2021SW002953. https://doi.org/10.1029/2021SW002953

Schwartz, S. J. (1998). Shock and discontinuity normals, mach numbers, and related parameters. *ISSI Scientific Reports Series*, *1*, 249–270.

Shi, X., Hartinger, M. D., Baker, J. B. H., Murphy, B. S., Bedrosian, P. A., Kelbert, A., & Rigler, E. J. (2022). Characteristics and sources of intense geoelectric fields in the United States: Comparative analysis of multiple geomagnetic storms. *Space Weather*, *20*(4), e2021SW002967. https://doi.org/10.1029/2021SW002967

Shue, J.-H., Song, P., Russell, C. T., Steinberg, J. T., Chao, J. K., Zastenker, G., et al. (1998). Magnetopause location under extreme solar wind conditions. *Journal of Geophysical Research*, *103*(A8), 17691–17700. https://doi.org/10.1029/98JA01103

Sibeck, D. G. (1990). A model for the transient magnetospheric response to sudden solar wind dynamic pressure variations. *Journal of Geophysical Research*, *95*(A4), 3755–3771. https://doi.org/10.1029/JA095iA04p03755

Smith, A. W., Rodger, C. J., Mac Manus, D. H., Rae, I. J., Fogg, A. R., Forsyth, C., et al. (2024). Sudden commencements and geomagnetically induced currents in New Zealand: Correlations and dependance. *Space Weather*, *22*(1), e2023SW003731. https://doi.org/10.1029/2023SW003731

Sonnerup, B. U. Ö., & Scheible, M. (1998). Minimum and maximum variance analysis. *ISSI Scientific Reports Series*, *1*, 185–220.

Trichtchenko, L. (2021). Frequency considerations in GIC applications. *Space Weather*, *19*(8), e2020SW002694. https://doi.org/10.1029/2020SW002694

Tsurutani, B. T., & Hajra, R. (2021). The interplanetary and magnetospheric causes of geomagnetically induced currents (GICs) > 10 A in the Mäntsälä Finland pipeline: 1999 through 2019. *J. Space Weather Space Clim.*, *11*, 23. https://doi.org/10.1051/swsc/2021001

Tu, C.-Y., & Marsch, E. (1995). MHD structures, waves and turbulence in the solar wind: Observations and theories. *Space Science Reviews*, *73*(1–2), 1–210. https://doi.org/10.1007/bf00748891

Viljanen, A., Koistinen, A., Pajunpää, K., Pirjola, R., Posio, P., & Pulkkinen, A. (2010). Recordings of geomagnetically induced currents in the Finnish natural gas pipeline–summary of an 11-year period. *Geophysica*, *46*(1–2), 59–67.

Winterhalter, D., Neugebauer, M., Goldstein, B. E., Smith, E. J., Bame, S. J., & Balogh, A. (1994). Ulysses field and plasma observations of magnetic holes in the solar wind and their relation to mirror-mode structures. *Journal of Geophysical Research*, *99*(A12), 23371–23381. https://doi.org/10.1029/94JA01977

Young, D. T., Burch, J. L., Gomez, R. G., De Los Santos, A., Miller, G. P., Wilson, P., IV, et al. (2016). Hot plasma composition analyzer for the magnetospheric multiscale mission. *Space Science Reviews*, *199*(1–4), 407–470. https://doi.org/10.1007/s11214-014-0119-6

Zhang, L., He, J., Zhao, J., Yao, S., & Feng, X. (2018). Nature of magnetic holes above ion scales: A mixture of stable slow magnetosonic and unstable mirror modes in a double-polytropic scenario? *The Astrophysical Journal*, *864*(1), 35. https://doi.org/10.3847/1538-4357/aad4aa

Zhang, T. L., Baumjohann, W., Russell, C. T., Jian, L. K., Wang, C., Cao, J. B., et al. (2009). Mirror mode structures in the solar wind at 0.72 au. *Journal of Geophysical Research*, *114*(A10), A10107. https://doi.org/10.1029/2009JA014103

Zheng, K., Boteler, D., Pirjola, R. J., Liu, L.-G., Becker, R., Marti, L., et al. (2014). Effects of system characteristics on geomagnetically induced currents. *IEEE Transactions on Power Delivery*, *29*(2), 890–898. https://doi.org/10.1109/TPWRD.2013.2281191

Zou, Y., Gjerloev, J. W., Ohtani, S., Friel, M., Liang, J., Lyons, L. L., et al. (2024). An extreme auroral electrojet spike during 2023 April 24th storm. *AGU Advances*, *5*(3), e2023AV001101. https://doi.org/10.1029/2023AV001101